

$\text{Li}_{4.3}\text{AlS}_{3.3}\text{Cl}_{0.7}$: a sulfide-chloride lithium ion conductor with a highly disordered structure

Jacinthe Gamon¹, Matthew S. Dyer^{1,3}, Benjamin B. Duff^{1,2}, Andrij Vasylenko¹, Luke M. Daniels¹, Michael W. Gaultois^{1,3}, Frédéric Blanc^{1,2,3}, John B. Claridge^{1,3} and Matthew J. Rosseinsky^{1,3}*

¹Department of Chemistry, University of Liverpool, Crown Street, L69 7ZD Liverpool, UK.

²Stephenson Institute for Renewable Energy, University of Liverpool, Peach Street, L69 7ZF Liverpool, UK.

³Leverhulme Research Centre for Functional Materials Design, Materials Innovation Factory, University of Liverpool, UK

KEYWORDS mixed anion, Li electrolyte, disorder, Ab Initio Molecular Dynamics, Maximum Entropy Method

ABSTRACT

Mixed anion materials and anion doping are very promising strategies to improve solid-state electrolyte properties by enabling an optimized balance between good electrochemical stability and high ionic conductivity. In this work, we present the discovery of a novel lithium aluminum sulfide-chloride phase. The structure is strongly affected by the presence of chloride anions on the sulfur site, as this stabilizes a higher symmetry phase presenting a large degree of cationic site

disorder, as well as disordered octahedral lithium vacancies, in comparison with Li-Al-S ternaries. The effect of disorder on the lithium conductivity properties was assessed by a combined experimental-theoretical approach. In particular, the conductivity is increased by a factor 10^3 compared to the pure sulfide phases. Although it remains moderate ($10^{-6} \text{ S}\cdot\text{cm}^{-1}$), Ab Initio Molecular Dynamics and Maximum Entropy (applied to neutron diffraction data) methods show that disorder leads to a 3D diffusion pathway, where Li atoms move thanks to a concerted mechanism. An understanding of the structure-property relationships is developed to determine the limiting factor governing lithium ion conductivity. This analysis, added to the strong step forward obtained in the determination of the dimensionality of diffusion paves the way for accessing even higher conductivity in materials comprising an *hcp* anion arrangement.

1. Introduction

Lithium ion battery technology is widely used in portable devices, electronic vehicles, as well as energy storage systems for national grid storage.^{1,2} All-solid-state batteries represent a significant advancement in this technology with the potential to use lithium metal as the anode alongside inorganic solid-state electrolytes. The latter have grown as a promising solution for preventing safety hazards originating from liquid electrolyte solvent flammability in lithium batteries. Overcoming the intrinsic lower ionic conductivity of solids compared to liquids as well as meeting the requirement for electrochemical stability *vs.* electrodes are the two main challenges for finding a viable candidate. Incredible progress in this direction has been made in recent years.³⁻⁵ The room temperature lithium conductivity target of $10^{-3} \text{ S}\cdot\text{cm}^{-1}$ has now been met in different families of materials, including, garnet type $\text{Li}_{6.55+y}\text{Ga}_{0.15}\text{La}_3\text{Zr}_{2-y}\text{Sc}_y\text{O}_{12}$ ($1.8 \times 10^{-3} \text{ S}\cdot\text{cm}^{-1}$),⁶ glass-ceramic $70 \text{ Li}_2\text{S} - 30 \text{ P}_2\text{S}_5$ (mol %) ($1.7 \times 10^{-2} \text{ S}\cdot\text{cm}^{-1}$),⁷ thio-LISICON $\text{Li}_{9.54}\text{Si}_{1.74}\text{P}_{1.44}\text{S}_{11.7}\text{Cl}_{0.3}$ ($2.5 \times 10^{-2} \text{ S}\cdot\text{cm}^{-1}$),⁸ and Li_3YBr_6 ($1.7 \times 10^{-3} \text{ S}\cdot\text{cm}^{-1}$).⁹ However, these materials still suffer from limitations such as high production and device processing costs (oxides garnets), sensitivity to moisture and air (sulfides), poor compatibility to cathode materials (hydrides), and low oxidation potential (halides). Developing innovative exploratory chemistry to access new functional lithium solid-state electrolytes that combine desirable materials characteristics needed for particular applications is therefore still very much at stake.

Research on mixed anion materials is expanding significantly and presents as an original way to modulate structure and properties in many fields of material science.^{10,11} While multiple anion chemistry is less understood and explored than multiple cation, single anion chemistry, even this restricted chemistry to date has afforded promising materials offering the stabilization of disordered phases and improved conductivity properties.¹²⁻¹⁸ Examples include the lithium

phosphorus oxynitride (LiPON), which is known for its outstanding electrochemical performance^{19,20}, and more recently, the lithium argyrodite family has received particular attention. In these compounds, the pure sulfide phase Li₇PS₆ presents an orthorhombic unit cell at room temperature, and the incorporation of halide anion leads to the stabilization of the cubic polymorph Li₆PS₅X (X = Cl, Br, I) with high lithium mobility.²¹ Recently, Morscher *et al.* showed that the Li-Si-O-Cl phase field includes new lithium hexagonal argyrodites, complementing the important cubic argyrodite family of lithium solid electrolytes, with Li₆SiO₄Cl₂ showing an order-disorder transition accompanied by an increase in Li conductivity.¹⁸ New ternary compounds, Li₅AlS₄ and Li₃AlS₃,^{22,23} were recently found in the Li-Al-S phase field, but these showed however low conductivity ($\approx 10^{-9}$ S cm⁻¹) resulting from highly ordered lithium and vacant sites. Exploring mixed anion chemistry is of high interest to evaluate the possibility of improving conductivity in these materials.

In this work, we report on the synthesis of a new lithium and aluminum mixed anion sulfide-chloride material of composition Li_{5-y}Al_{1+(y-x)/3}S_{4-x}Cl_x (x = 0.5 - 0.7; y = 0.5 - 1) with a highly disordered structure. The in-depth characterization of Li_{4.3}AlS_{3.3}Cl_{0.7} shows considerable improvement of the lithium conductivity properties compared to the mono-anionic sulfide parent phase. The effect of mixed anion and disorder on the ionic conductivity is studied by a combined experimental-computational approach.

2. Experimental Section

2.1. Synthesis

Samples with compositions $\text{Li}_{5-x}\text{AlS}_{4-x}\text{Cl}_x$ ($x = 0.3; 0.5; 0.7; 1$), $\text{Li}_5\text{Al}_{1-x/3}\text{S}_{4-x}\text{Cl}_x$ ($x = 0.15; 0.5; 0.7$), $\text{Li}_{3-x}\text{AlS}_{3-x}\text{Cl}_x$ ($x = 0.05; 0.1; 0.2; 0.4$) and $\text{Li}_3\text{Al}_{1-x/3}\text{S}_{3-x}\text{Cl}_x$ ($x = 0.2; 0.4; 0.5$) were made by solid state synthesis. Stoichiometric amounts of Li_2S (Merck, 99.98 %), Al_2S_3 (Alfa Aesar, 99+ %) and LiCl (Merck, 99.99 %) powder were weighted in order to yield a total mass of powder of 300 mg. For the title compound $\text{Li}_{4.3}\text{AlS}_{3.3}\text{Cl}_{0.7}$, 158 mg of Li_2S , 108 mg of Al_2S_3 , and 34 mg of LiCl were weighted. Powders were combined and mixed thoroughly in an agate mortar for 15 min, transferred in an alumina crucible and then sealed in a quartz tube with Ar under a pressure of 10^{-4} mbar. The tube containing the sample was heated to 700 °C at a ramp rate of $5\text{ °C}\cdot\text{min}^{-1}$, held at 700 °C for 12 hours, and then cooled to room temperature at a ramp rate of $5\text{ °C}\cdot\text{min}^{-1}$. The resulting powder was then manually ground in order to obtain a fine powder. Precursors and resulting powders were handled in an Ar-filled glovebox.

2.2. Elemental analysis

Elemental analysis of $\text{Li}_{4.3}\text{AlS}_{3.3}\text{Cl}_{0.7}$ was performed by Mikroanalytisches Labor Pascher at Remagen-Bandorf, Germany, after dissolution in a HF/HCl solution at elevated temperature and pressure.

2.3. Diffraction

Routine analysis of phase purity and lattice parameters were performed on a Bruker D8 Advance diffractometer with a monochromated Cu source ($\text{K}\alpha_1$, $\lambda = 1.54060\text{ \AA}$) or on a Rigaku SmartLab diffractometer with monochromated Mo source ($\text{K}\alpha_1$, $\lambda = 0.70932\text{ \AA}$) in powder transmission Debye Scherrer geometry (capillary) with sample rotation. Synchrotron X-ray diffraction (SXRD) was performed at the I11 beamline at Diamond Light Source (Oxfordshire, U.K.), with an incident wavelength of 0.825186 \AA using a wide-angle position sensitive detector, and samples sealed in

$\varnothing = 0.5$ mm glass capillaries to prevent air exposure. Time-of-flight (ToF) neutron powder diffraction (NPD) data was collected at room temperature using the Polaris instrument at ISIS neutron source (Oxfordshire, U.K.). Samples were loaded in $\varnothing = 6$ mm vanadium cylindrical cans and sealed in an Argon-filled glovebox.

The structural models were refined by the Rietveld method as implemented in the FullProf suite.²⁴ Peak shapes were modelled using the Thompson-Cox-Hastings function and the T.O.F. pseudo-Voigt back-to-back exponential function with spherical harmonic expansion for SXRD and NPD data, respectively. For the sake of realism, all uncertainties were increased by Berar's factor²⁵ (3.2, 5.9, 4.7, 4.6, 3.1 for SXRD, NPD Bank 2, NPD Bank 3, NPD Bank 4, and NPD Bank 5, respectively according to FullProf).

2.4. AC Impedance spectroscopy

Pellets were made by uniaxial pressing 30-100 mg of powder in a 5 or 8 mm diameter cylindrical steel die at a pressure of 125 MPa. Pellets were then sintered at 700 °C for 12 h in an evacuated quartz tube. A relative density of 85 % was obtained by this method.

AC impedance measurements were performed using an impedance analyser (Solartron 1296 dielectric interface coupled with the Solartron 1255B frequency response analyser) in the frequency range from 1 MHz to 100 mHz (with an amplitude of 50 mV). Silver paint (RS silver conducting paint 186-3600), brushed on both sides of the pellet and dried under vacuum at room temperature, was used as ion blocking electrodes. Variable temperature conductivity measurements were carried out under argon (flow rate 50 mL·min⁻¹), using a custom built sample holder, in the temperature range 25-125 °C. The impedance spectra were fitted with an equivalent circuit using the ZView2 program.²⁶

2.5. NMR

$\text{Li}_{4.3}\text{AlS}_{3.3}\text{Cl}_{0.7}$ was packed into a 3.2 mm zirconia rotor in an Ar-filled glovebox and ^6Li and ^{27}Al Magic Angle Spinning (MAS) NMR spectra recorded using a 3.2 mm HXY MAS Probe in double resonance mode on a 20 T Bruker NEO solid-state NMR spectrometer under MAS at a rate of $\omega_r/2\pi = 20$ kHz. ^6Li spectra were recorded with a pulse length of 3 μs at a radiofrequency (rf) field amplitude of $\omega_1/2\pi = 83$ kHz. ^{27}Al spectra were obtained with a short pulse angle of 30° of duration 0.2 μs duration at an rf amplitude of $\omega_1/2\pi = 50$ kHz. The ^{27}Al triple quantum magic-angle spinning (MQMAS)²⁷ was obtained with a z -filtered sequence²⁸ and using rf field amplitudes of $\omega_1/2\pi = 50$ kHz for the excitation and reconversion pulses and 20 kHz for the selective 90° pulse. All data acquisitions were quantitative using recycle delays longer than five-times the spin-lattice relaxation times, T_1 (measured using a standard saturation recovery sequence). All ^6Li and ^{27}Al shifts were referenced to 10 M LiCl in D_2O and 0.1 M $\text{Al}(\text{NO}_3)_3$ in H_2O at 0 ppm, respectively.

2.6. Thermodynamical phase stability calculations

Starting from the experimentally established ordered crystal structure of Li_3AlS_3 ,²³ we applied the crystal structure prediction code ChemDASH to establish a model of an ordered Cl-doped crystal structure $\text{Li}_{13}\text{Al}_3\text{S}_{10}\text{Cl}_2$ (corresponding to $\text{Li}_{4.3}\text{AlS}_{3.3}\text{Cl}_{0.7}$). Geometry optimization of the structures was performed with Density-Functional Theory (DFT) as implemented in VASP:²⁹ with 700 eV for kinetic energy cutoff of the plane waves, PBE pseudopotentials³⁰ and $5 \times 5 \times 5$ k-points grid till forces on atoms were less than 0.001 eV/Å.

From the disordered structures $\text{Li}_{4.3}\text{AlS}_{3.3}\text{Cl}_{0.7}$ obtained experimentally, we created two disordered structural analogues with composition Li_5AlS_4 and Li_3AlS_3 : i) the mixed S/Cl site was replaced by fully occupied S sites only, ii) in Li_5AlS_4 , the octahedral lithium site, Li2, was set to a full

occupancy and iii) in Li_3AlS_3 ($= \text{Li}_4\text{Al}_{4/3}\text{S}_4$), the site occupancy factors (*sof*) of Al and Li1 were set to 0.33 and 0.42, respectively. This enabled to match the stoichiometry of both compounds. We then created supercells of the three disordered compounds³¹ and ranked all possible atomic configurations according to their Coulomb energy. For the top 100 structures in this list, we performed DFT geometry optimization and identified the lowest energy structures.

The Gibbs' free energy of the ordered and disordered structures of $\text{Li}_{4.3}\text{AlS}_{3.3}\text{Cl}_{0.7}$, Li_5AlS_4 and Li_3AlS_3 was calculated as:

$$G = H - TS, \quad (\text{Equation 1})$$

where H is enthalpy of a structure calculated with DFT; T is temperature, and S is entropy of mixing (configurational entropy) calculated as follows:

$$S = -k \sum_i x_i \cdot \log x_i, \quad (\text{Equation 2})$$

where x_i is the mole concentration of the i^{th} component (atomic species) in the structure, and k is Boltzmann constant.

2.7. Ab Initio Molecular Dynamics (AIMD)

Two structures were generated as starting points for AIMD calculations. The first structure was chosen from 537 508 symmetrically inequivalent orderings of cations and anions generated using SimDope.³² Configurations with composition $\text{Li}_{13}\text{Al}_3\text{S}_{10}\text{Cl}_2$ ($\text{Li}_{4.33}\text{AlS}_{3.33}\text{Cl}_{0.67}$) were generated from a $2 \times 2 \times 2$ supercell of the experimental structure and avoiding having short Li-Li distances. From these, the 1797 structures in space group Cm were chosen to optimize with DFT since they were the highest symmetry structures. Geometry optimization was performed using VASP³³ with

the PBE functional,³⁰ a plane wave cutoff energy of 600 eV and a $2 \times 2 \times 1$ k -point grid until all forces fell below 0.02 eV \AA^{-1} . The lowest energy structure was then taken and used to generate a larger supercell with total composition $\text{Li}_{104}\text{Al}_{24}\text{S}_{80}\text{Cl}_{16}$ which was used to initialize the AIMD calculations.

The second structure was produced in a similar way by generating 45 513 structures using SimDope but starting with the metal and vacancy ordering present in the structure of $\text{Li}_{4.4}\text{Al}_{0.4}\text{Ge}_{0.6}\text{S}_4$.³⁴ The 728 structures with higher symmetry than PI were optimized as above and the lowest energy structure once again chosen to generate a larger supercell with total composition $\text{Li}_{104}\text{Al}_{24}\text{S}_{80}\text{Cl}_{16}$ for AIMD calculations.

Fixed cell AIMD calculations were carried out with the PBE functional,³⁰ a plane wave cutoff energy of 600 eV and Γ -point only sampling of reciprocal space. A timestep of 0.5 fs was used throughout. An initial temperature ramp from 0–400 K was carried out for 4 ps, followed by an equilibration period of 10 ps at 400 K in which temperature was controlled by velocity scaling at every step. A production run of 100 ps was then carried out for both structures at 400 K using a Nosé thermostat.³⁵

2.8. Maximum Entropy Method (MEM)

The maximum entropy method applied to diffraction data consists in optimizing the reconstruction of the scattering density from the observed structure factors by finding the maximum of the informational entropy under several constraints through an iterative procedure.³⁶ MEM is a powerful tool for reconstructing scattering density from incomplete and/or noisy data systems and limits termination effects obtained through usual Fourier synthesis, particularly important in disordered systems.³⁷ MEM applied to neutron diffraction data is useful to shed light on position

of light elements, such as Li, poorly visible with X-rays, but presenting large enough neutron scattering length. This method was recently used to describe conduction pathways in several ionic conductors of lithium^{38,39} and oxygen⁴⁰ in particular. Maximum entropy calculation was performed with the program Dysnomia⁴¹ using an input file containing observed structure factors from the NPD data of Bank 4 and generated by FullProf.²⁴ Visualization of nuclear densities and extraction of 2D displays was then performed in the program Vesta.⁴² Because the ⁷Li scattering length is negative ($b_{\text{Li}} = -2.22$ fm), visualization of negative levels is performed to view Li positions within the structure.

3. Result and discussion

3.1. Synthesis and structure determination

We studied chloride for sulfur substitution in recently reported compounds within the Li-Al-S phase field: Li_5AlS_4 ²² and Li_3AlS_3 .²³ The structure of these materials can be described as an *hcp*-type packing of sulfur anions within which cations occupy tetrahedral (Li and Al) and octahedral sites (Li only) in a highly ordered pattern.^{22,23}

Compositions were chosen along solid solution lines $\text{Li}_{5-x}\text{AlS}_{4-x}\text{Cl}_x$, $\text{Li}_5\text{Al}_{1-x/3}\text{S}_{4-x}\text{Cl}_x$, $\text{Li}_{3-x}\text{AlS}_{3-x}\text{Cl}_x$ and $\text{Li}_3\text{Al}_{1-x/3}\text{S}_{3-x}\text{Cl}_x$ (Figure 1a). For all compositions screened, reflections, which did not correspond to any known phases, appeared. These were attributed to a new phase (denominated phase A) which could then be isolated for four compositions along the solid solution lines $\text{Li}_{5-x}\text{AlS}_{4-x}\text{Cl}_x$ ($x = 0.5; 0.7$) and $\text{Li}_3\text{Al}_{1-x/3}\text{S}_{3-x}\text{Cl}_x$ ($x = 0.4; 0.5$). Figure S1a (Supporting Information, SI) shows the XRD diagram of these four samples, and the slight shift of the peak positions with Q (Figure S1b) attests for a variation of their lattice parameters depending on the composition. Higher or lower x values and/or moving along the solid solution lines $\text{Li}_5\text{Al}_{1-x/3}\text{S}_{4-x}\text{Cl}_x$ and Li_3 -

$x\text{AlS}_{3-x}\text{Cl}_x$ resulted in the formation of mixed phase compounds (example shown along the $\text{Li}_3\text{Al}_{1-x/3}\text{S}_{3-x}\text{Cl}_x$ solid solution line on Figure S2). The screening resulted in the delimitation of a small range of compositions for the formation of phase A with high purity (light red area on Figure 1a).

This new phase could be indexed to the $P\bar{3}m1$ space group (Le Bail fit on Figure S1a for composition $\text{Li}_{4.3}\text{AlS}_{3.3}\text{Cl}_{0.7}$, with $a = 3.93161(3) \text{ \AA}$ and $c = 6.23971(3) \text{ \AA}$). All lattice parameters and cell volumes are reported in Table S1. The cell volume increases when the lithium to total cation ratio increases, consistent with the larger ionic radius of lithium (0.59 \AA (IV) and 0.76 \AA (VI)) compared to aluminum (0.53 \AA (IV)), as shown on Figure 1b.⁴³ Interestingly, this cell directly relates to that of Li_2FeS_2 ($P\bar{3}m1$, $a = 3.902(1) \text{ \AA}$, $c = 6.294(2) \text{ \AA}$),⁴⁴ whose structure can be viewed as a cation disordered analogue of Li_5AlS_4 and Li_3AlS_3 (Figure S3b,c,d). This seems promising for promoting ionic conduction and call for further structural investigation.

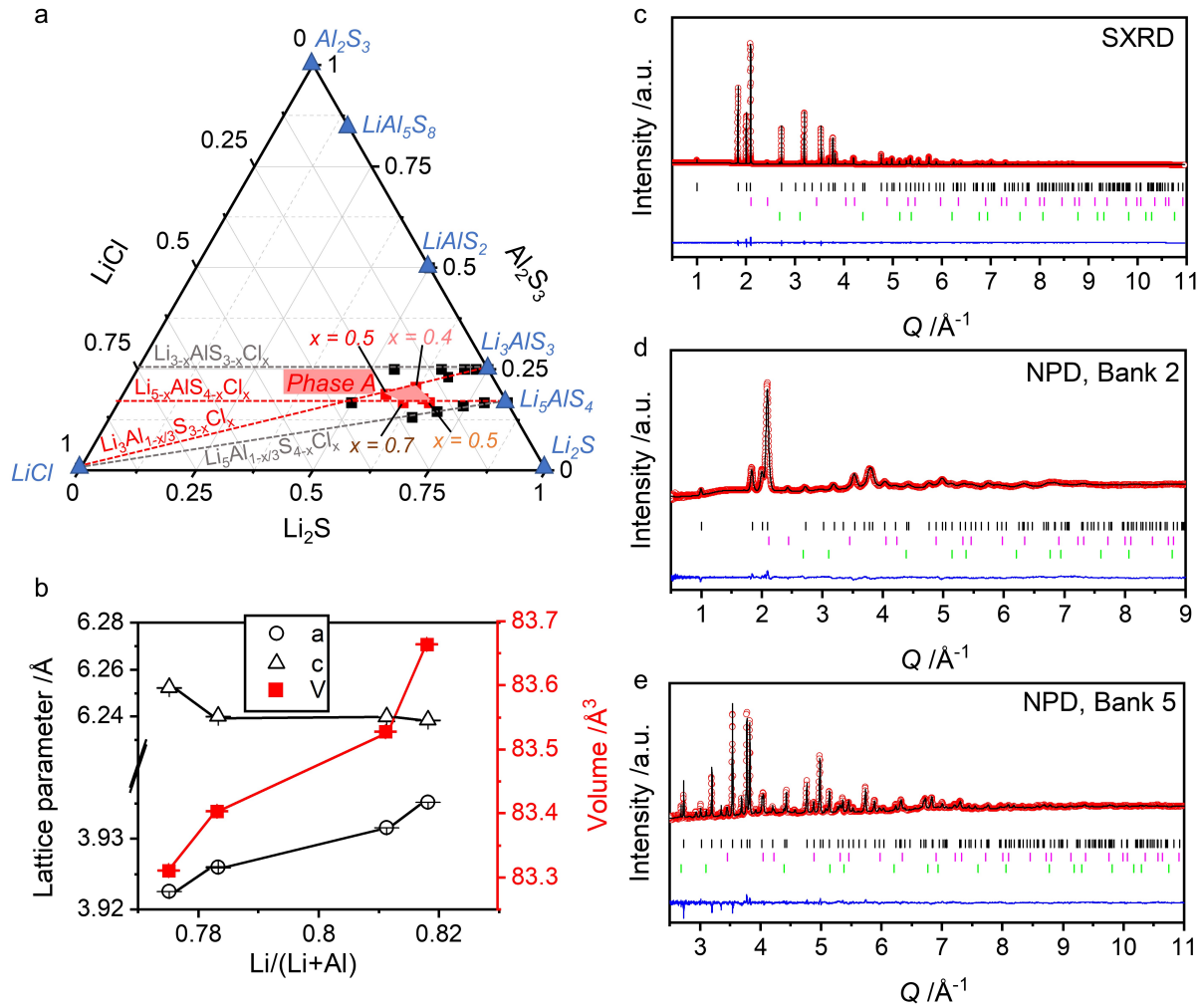


Figure 1. (a) Screening of S for Cl substitution in Li_3AlS_3 and Li_5AlS_4 following the four solid solution lines: $Li_{5-x}AlS_{4-x}Cl_x$, $Li_5Al_{1-x/3}S_{4-x}Cl_x$, $Li_{3-x}AlS_{3-x}Cl_x$ and $Li_3Al_{1-x/3}S_{3-x}Cl_x$. Known materials are represented by blue triangles, attempted compositions which resulted in mixed phase compounds by black squares and compositions which lead to the new phase A with high purity by red squares. (b) Lattice parameters of phase A in function of the amount of lithium. (c, d, e) Final Rietveld fit against (c) the SXR data ($\lambda = 0.825186 \text{ \AA}$, Diamond, UK), and the NPD data from (d) Bank 2 ($2\theta = 25.990^\circ$) and (e) Bank 5 ($2\theta = 146.720^\circ$) of Polaris instrument (ISIS, UK), with I_{obs} (red dots), I_{calc} (black line), $I_{obs}-I_{calc}$ (blue line), and Bragg reflections (black tick marks for $Li_{4.3}AlS_{3.3}Cl_{0.7}$, pink tick marks for LiCl ($\sim 2 \text{ w\%}$) and green tick marks for Al ($\sim 1 \text{ w\%}$)).

An in-depth structural study, combining synchrotron X-ray diffraction (SXR) and neutron powder diffraction (NPD), was performed on one of these compositions: $Li_{4.3}AlS_{3.3}Cl_{0.7}$, corresponding to $x = 0.7$ in $Li_{5-x}AlS_{4-x}Cl_x$. Small quantity of Al metal and LiCl impurities were

identified through preliminary Pawley refinement, and these phases were added to the Rietveld refinement.

The Li_2FeS_2 ($\text{Li}_4\text{Fe}_2\text{S}_4$ for compositional analogy) structure (Figure S3b) was used as a starting model where 1/6 of the S sites are occupied by Cl atoms (Wyckoff position $2d$), Fe atoms are replaced by Al atoms with a site occupancy factor (*sof*) divided by 2 (Wyckoff position $2d$, *sof* = 0.25) and the Li atoms distributed among the Al tetrahedral site (Li1, *sof* = 0.75) and the octahedral site (Li2, Wyckoff position $1a$, *sof* = 0.5). This starting model showed a good fit to the SXRD data but fit poorly the NPD data at high Q (Figure S4a), pointing towards different Li site occupation, not well-determined using X-ray radiation. The Fourier difference map of Bank 5 of the NPD data highlighted a scattering density deficiency at the position $(1/3, 2/3, 0.85)$ while showing an excess scattering density on the Al/Li1 site (Figure S4b). The latter was then split into two sites of different z position. Eventually, positions, site occupancy factors and anisotropic displacement parameters of all atoms were simultaneously refined against the combined SXRD and NPD data, showing a good fit to all datasets (Figure 1c, d, e and Figure S5) and yielding the final model. The outcome of the refinement is presented in Table S2, S3 and S4. The overall composition refines to $\text{Li}_{4.32(1)}\text{AlS}_{3.308(4)}\text{Cl}_{0.71(2)}$, close to the chemical composition measured by elemental analysis, $\text{Li}_{4.36(4)}\text{Al}_{1.08(1)}\text{S}_{3.30(3)}\text{Cl}_{0.67(1)}$, for which the slight deviation can be attributed to the presence of the Al metal and LiCl impurities (~1 and 2 w%, respectively, according to quantitative phase analysis with FullProf). The compound will be denoted $\text{Li}_{4.3}\text{AlS}_{3.3}\text{Cl}_{0.7}$ hereafter for simplicity.

3.2. Structure description

The structure consists of an anion sublattice in a *hcp* type packing arrangement. Sulfur and chlorine atoms are distributed randomly among the single anionic site in a S/Cl ratio of $0.827(3) / 0.178(7)$,

yielding a highly disordered structure. Cations occupy interstitial sites in between two anion slabs so that the structure exhibits two distinct layers alternating along the c axis (Figure 2a). In the first layer, lithium atoms partially occupy the octahedral (Li2, *sof* of 0.644(2)) and tetrahedral (Li3, *sof* of 0.260(2)) interstices (Figure 2b). In between the next two anion slabs, the two cations are randomly distributed among the T^+ and T^- tetrahedral sites only, so that aluminum and lithium (Li1) are present in a Al/Li = 0.25/0.499(2) ratio (Figure 2c). This layer forms a “pure” tetrahedral layer. This layered structure type adopted by $\text{Li}_{4.3}\text{AlS}_{3.3}\text{Cl}_{0.7}$ (as well as Li_3AlS_3 , Li_5AlS_4 and Li_2FeS_2) is distinct from the wurtzite structure, in which all layers are the same, with occupation by cations of T^+ tetrahedra only.

In the “Li-only” polyhedral layer, Li2 octahedra are connected to six Li3 tetrahedra and six other Li2 octahedra of the layer via face and edge sharing, respectively (Figure 2b). The other two faces of the octahedra are part of the sulfur slab delimiting the layer and are connected to the fully vacant octahedral interstices of the tetrahedral layers above and below (Figure 2a).

Each T^+ (T^-) Al/Li1 tetrahedra is connected via edge sharing to the surrounding three T^- (T^+) tetrahedra of the layer (Figure 2c). It is connected to the consecutive layers by sharing its three remaining edges (from the base) and one corner (the apex), with the Li2 octahedra from the above and below polyhedral layer, respectively (Figure 2a). The face of the base and the apex of each of these tetrahedra are also shared with that of the below and above Li3 tetrahedra, respectively (Figure 2a,d). These two face-shared tetrahedra form a unit, in which the hypothetical Al-Li3 and Li1-Li3 distances are very small ($d_{\text{Al-Li3}} = 1.543(13)$ Å and $d_{\text{Li1-Li3}} = 1.274(14)$ Å, Figure 2d), rendering their mutual occupation within the same unit very unlikely. The combined site occupancy factor of the unit refines to 1.009(4), very close to a full occupancy, suggesting that the

unit hosts exactly one atom, and no vacancies. As such, disordered vacancies are distributed among Li2 octahedral sites only ($sof_{Li2} = 0.644(2)$).

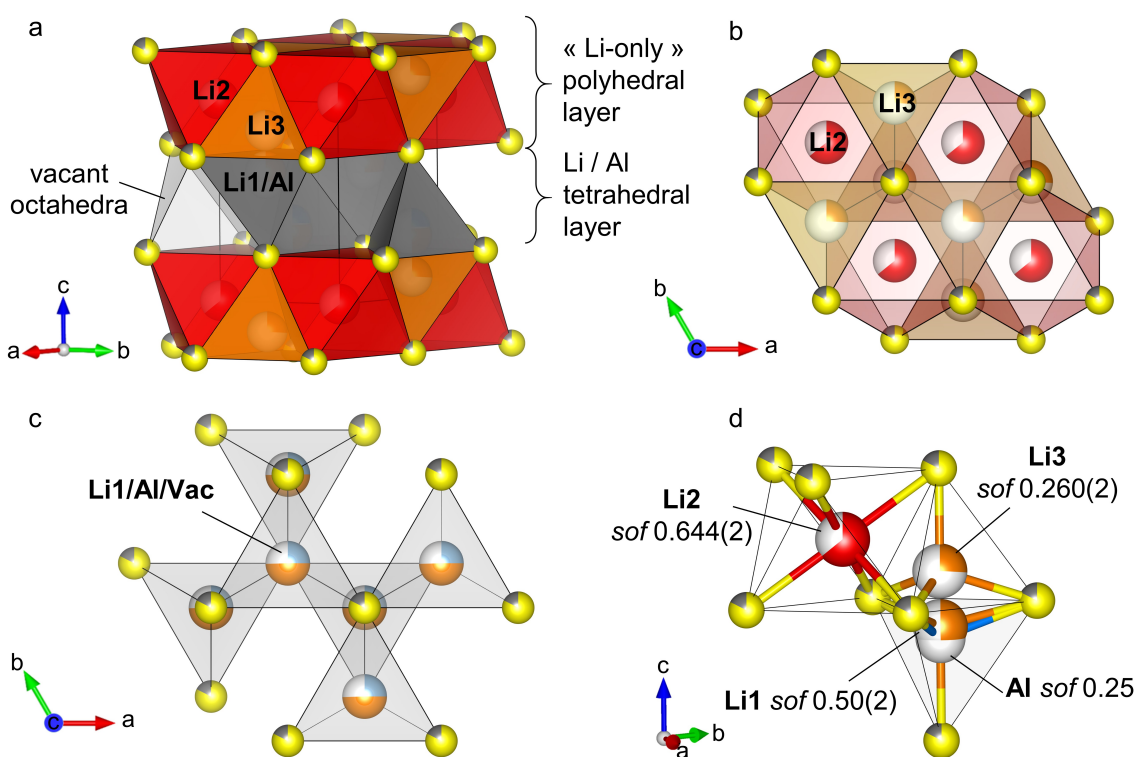


Figure 2. Crystal structure of $Li_{4.3}AlS_{3.3}Cl_{0.7}$, with sulfur (yellow sphere) and chlorine (grey sphere) sharing the same site and arranged in a *hcp* type packing, Li atoms occupying octahedral (red) and tetrahedral (orange) interstices in the first layer, while Al (blue sphere) and remaining Li (orange sphere) atoms are randomly distributed among the tetrahedral interstices (grey) in the consecutive layers. (a) Layered view, (b) “Li-only” polyhedral layer in the (*ab*) plane, (c) tetrahedral layer in the (*ab*) plane and (d) polyhedral coordination.

Multinuclear 6Li and ^{27}Al NMR spectra were recorded to further support the structural refinement.

The 6Li MAS NMR spectrum (Figure 3a) displays an intense resonance at 1 ppm assigned to tetrahedral and octahedral sites from the $Li_{4.3}AlS_{3.3}Cl_{0.7}$ phase and a small peak at ~ -0.3 ppm, which could be attributed to small amounts of octahedral lithium sites from the ordered Li_3AlS_3 phase.²³ A smaller peak at -1.1 ppm is also visible and corresponds to solid $LiCl^{45}$ (observed in XRD). The main signal is narrow (50 Hz) at room temperature and suggests the presence of a

motionally averaged NMR signal arising from fast Li^+ hops and preventing the spectral resolution of Li sites with various coordination numbers. The ^{27}Al MAS NMR spectrum (Figure 3b) shows the presence of two asymmetrically broadened and overlapping peaks around 125 ppm which are assigned to Al tetrahedra based on the shift value (note that the quadrupolar induced shift⁴⁶ is likely smaller than 5 ppm at this magnetic field). Less intense resonances at 70 and 16 ppm (Figure S6) are assigned to a small amount of more highly coordinated Al. The broadening arises from second-order quadrupolar interaction coming from deviation from the perfect tetrahedral site symmetry while the low frequency tail is caused by a distribution of quadrupolar couplings stemming from local structural disorder (see below). Attempt to resolve the main resonances using a ^{27}Al MQMAS NMR experiment only confirms this distribution and no improvement in the resolution of the corresponding ^{27}Al isotropic spectrum is observed. This is in sharp contrast to the clear second-order quadrupolar line shape observed in the ^{27}Al NMR spectrum of the parent ordered Li_3AlS_3 ²³ that illustrated the lack of disorder.

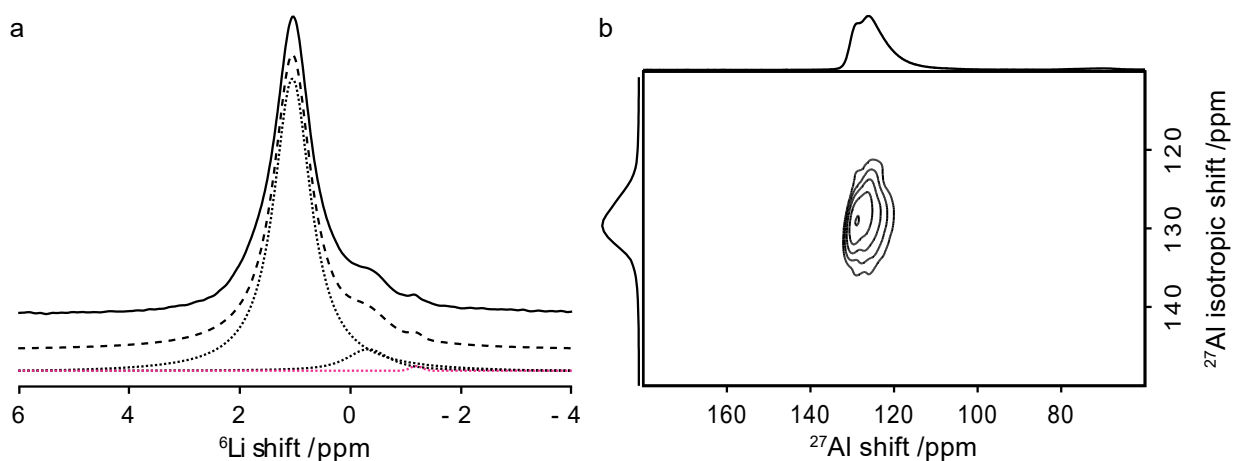


Figure 3. (a) ^6Li MAS spectrum of $\text{Li}_{4.3}\text{AlS}_{3.3}\text{Cl}_{0.7}$. The experimental spectrum (full line), total fit (dashed line) spectral deconvolution (dotted lines) are also shown. (b) ^{27}Al MQMAS of $\text{Li}_{4.3}\text{AlS}_{3.3}\text{Cl}_{0.7}$. The spectrum on the top is the ^{27}Al MAS NMR spectrum, while the one on the left is the isotropic ^{27}Al spectrum free of anisotropic broadening.

As expected from a simple S to Cl substitution mechanism, the backbone of the parent material structures, Li_5AlS_4 and Li_3AlS_3 , is maintained for the substituted phase $\text{Li}_{4.3}\text{AlS}_{3.3}\text{Cl}_{0.7}$. The three structures present an *hcp* type packing of anions (either S^{2-} only or a random distribution $\text{S}^{2-}/\text{Cl}^-$), and alternating tetrahedral Al/Li layers with Li-only polyhedral layers. Indeed, the similarity in the ionic radius of Cl^- (1.81 Å) and S^{2-} (1.84 Å) is favorable to site sharing and therefore helps to maintain structural integrity (Figure S3a, c, d).

However, the cation arrangement within each layer is considerably different in the pure sulfide and in the sulfide-chloride phases, so that Li_5AlS_4 and Li_3AlS_3 are superstructures of $\text{Li}_{4.3}\text{AlS}_{3.3}\text{Cl}_{0.7}$. In Li_5AlS_4 , Al and Li are ordered among the tetrahedral interstices of the tetrahedral layer in a 1:3 arrangement, and the octahedral sites of the “Li-only” layer are fully occupied. In Li_3AlS_3 , in the tetrahedral layer, Al, Li and vacancies are ordered in a 1:1:1 arrangement and 2/3 of the octahedral interstices are occupied in the Li-only layer, so that this structure presents a high proportion of ordered vacancies in both the tetrahedral and Li-only layer. The presence of Cl in the structure promotes the formation of a higher symmetry phase, with a high degree of site disorder, as well as the presence of disordered vacancies, which is expected to have a major impact on the Li mobility.

3.3.Phase stability calculation

Such disorder is absent in the pure sulfide compositionally related phases Li_5AlS_4 and Li_3AlS_3 which calls for an understanding of the effect of Cl^- substitution on the formation of disorder in this structure type. The Gibb’s free energy of Li_5AlS_4 , Li_3AlS_3 and $\text{Li}_{4.3}\text{AlS}_{3.3}\text{Cl}_{0.7}$ materials in their hypothetical ordered (G_o) and disordered (G_d) structure was calculated (*cf.* Experimental section). The Gibbs free energy deviation: $\Delta G = G_o - G_d$ indicates whether the ordered (if $\Delta G > 0$)

or disordered (if $\Delta G < 0$) structure is more energetically favorable at a given temperature. In Li_5AlS_4 and Li_3AlS_3 , ΔG is negative at $T > 1190$ °C and $T > 688$ °C, respectively, whereas for $\text{Li}_{4.3}\text{AlS}_{3.3}\text{Cl}_{0.7}$, ΔG is negative at $T > 250$ °C. This decrease in temperature is due to the contribution of configurational entropy (*cf.* $G(T)$ plots in the SI, Figure S7). In these calculations, the contribution from the vibrational entropy was not taken into account, which impedes direct comparison of theoretically obtained free energy values for these compositions. However, the significant reduction in transition temperature, close to room temperature, indicates that, via increased mixing entropy, Cl doping facilitates thermodynamic stabilization.

3.4. Lithium ionic conductivity

The lithium ionic conductivity was measured by AC impedance spectroscopy on a sintered pellet. The room temperature Nyquist plots of $\text{Li}_{4.3}\text{AlS}_{3.3}\text{Cl}_{0.7}$ and $\text{Li}_{4.5}\text{AlS}_{3.5}\text{Cl}_{0.5}$ are presented on Figure 4a. The presence of the two semicircles is characteristics of the deconvolution of two diffusion phenomena occurring on different time scales: bulk conductivity and conductivity through grain boundaries. The plot was therefore fitted using a typical equivalent circuit presented in the inset of Figure 4a to take into account these two contributions and obtain the conductivities. The room temperature bulk and total conductivity are $\sigma_{\text{bulk}}(303 \text{ K}) = 6.1(6) \times 10^{-6} \text{ S}\cdot\text{cm}^{-1}$ and $\sigma_{\text{tot}}(303 \text{ K}) = 2.5(2) \times 10^{-6} \text{ S}\cdot\text{cm}^{-1}$, respectively for $\text{Li}_{4.3}\text{AlS}_{3.3}\text{Cl}_{0.7}$ and $\sigma_{\text{bulk}}(303 \text{ K}) = 8.1(9) \times 10^{-6} \text{ S}\cdot\text{cm}^{-1}$ and $\sigma_{\text{tot}}(303 \text{ K}) = 3.7(4) \times 10^{-6} \text{ S}\cdot\text{cm}^{-1}$, respectively for $\text{Li}_{4.5}\text{AlS}_{3.5}\text{Cl}_{0.5}$. These values are very close showing that the amount of lithium does not have major impact on the conductivity.

AC impedance was measured on both samples over the temperature range 24 – 125 °C, and each Nyquist plot was fitted using the same equivalent circuit. σ_{bulk} was extracted at each temperature

point and showed to follow the Arrhenius law, with activation energy, E_a , of 0.33(1) eV and 0.35(1) eV for $\text{Li}_{4.3}\text{AlS}_{3.3}\text{Cl}_{0.7}$ and $\text{Li}_{4.5}\text{AlS}_{3.5}\text{Cl}_{0.5}$, respectively (Figure 4b).

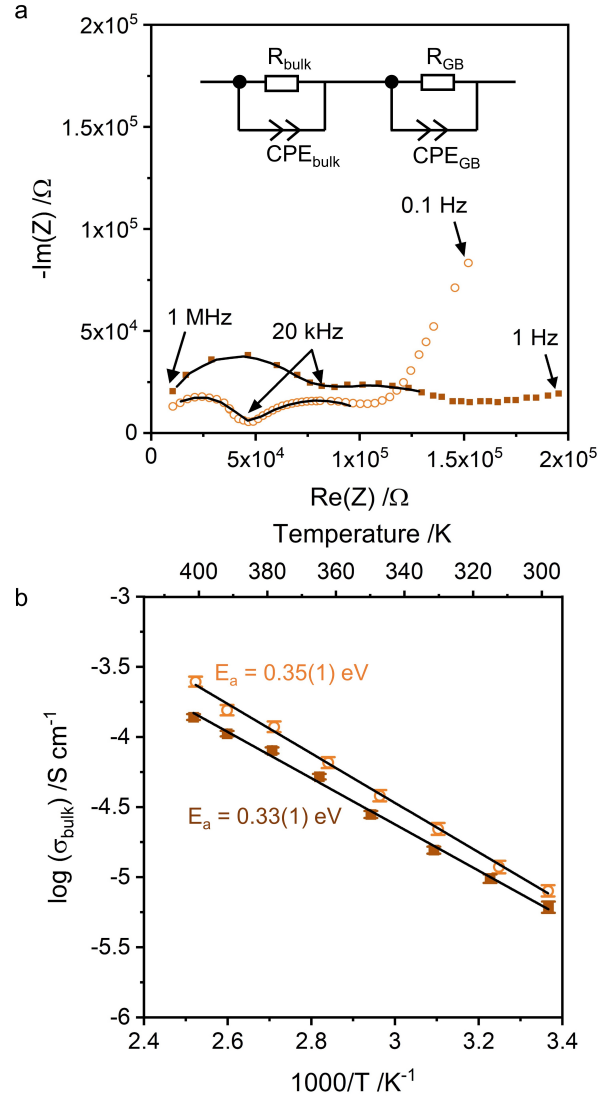


Figure 4. (a) Room temperature (303 K) Nyquist plot of $\text{Li}_{4.3}\text{AlS}_{3.3}\text{Cl}_{0.7}$ (filled brown squares) and $\text{Li}_{4.5}\text{AlS}_{3.5}\text{Cl}_{0.5}$ (empty orange circles) and their fit using the equivalent circuit in inset (black line), showing the two contributions to the conductivity, and (b) Arrhenius plot of the bulk conductivity of the two samples measured by AC impedance, and the linear fit using Arrhenius law (black line). CPE stand for Constant Phase Element, R for resistance and GB for Grain Boundary.

Compared to the pure sulfide materials Li_5AlS_4 and Li_3AlS_3 , which showed room temperature conductivity of $\sigma_{\text{tot}} = 9.7 \times 10^{-9} \text{ S} \cdot \text{cm}^{-122}$ and $\sigma_{\text{bulk}} = 1.3(1) \times 10^{-8} \text{ S} \cdot \text{cm}^{-1,23}$ respectively, the Li

bulk mobility is increased by almost three orders of magnitude in the mixed chloride-sulfide phases. Concomitantly, the activation energy decreases by 30 to 40 %, with $E_a = 0.61$ eV for Li_5AlS_4 ²² and $E_a = 0.48$ eV for Li_3AlS_3 .²³

Likewise, Leube *et al.* recently reported a major conductivity increase in this structure type, thanks to the introduction of a 4+ charged cation in the pure sulfide phase Li_5AlS_4 .³⁴ The bulk conductivity of $\text{Li}_{4.4}\text{Al}_{0.4}\text{Ge}_{0.6}\text{S}_4$ in particular, is at least as high as the reported total conductivity $\sigma_{\text{tot}} = 4.3(3) \times 10^{-5} \text{ S}\cdot\text{cm}^{-1}$. The conductivity increase compared to Li_5AlS_4 or Li_3AlS_3 was attributed to the presence of disordered vacancies among the lithium sites while maintaining the highly ordered anion S^{2-} sublattice and the site differentiation between Li^+ and non-mobile cations.³⁴ The conductivity of $\text{Li}_{4-x}\text{AlS}_{3-x}\text{Cl}_x$ ($x = 0.5 ; 0.7$) remains in the same conductivity range as the $\text{Li}_{4.4}\text{M}_{0.4}\text{M}'_{0.6}\text{S}_4$ ($M = \text{Al, Ga}; M' = \text{Ge, Sn}$) compounds, while being one order of magnitude lower than that of the best material in the series, $\text{Li}_{4.4}\text{Al}_{0.4}\text{Ge}_{0.6}\text{S}_4$.

In order to find an explanation for the observed differences and similarities in the Li mobility of these materials, the study of the diffusion mechanism was undertaken.

3.5. Lithium diffusion pathways

In order to visualize conduction pathways, Ab Initio Molecular Dynamics (AIMD) was conducted on the highest symmetry and most stable structure generated from a ($2a, 2b, 2c$) supercell of the $\text{Li}_{4.3}\text{Al}_{3.3}\text{S}_{3.3}\text{Cl}_{0.7}$ experimental structure (*cf.* Experimental Section). The structure is shown in Figure S8 and presents the overall composition $\text{Li}_{13}\text{Al}_3\text{S}_{10}\text{Cl}_2$ ($\text{Li}_{4.3}\text{AlS}_{3.3}\text{Cl}_{0.7}$). As the experimental structure does, it consists of tetrahedral layers containing Al and Li, alternating with “Li-only” layers. One “Li-only” layer (the one in the center of the cell) shows fully occupied octahedral sites and fully vacant tetrahedral sites. It is bounded by pure sulfide layers above and

below it. The other “Li-only” layer (the one at the bottom/top) has two octahedral sites and four tetrahedral sites occupied, leaving four octahedral sites vacant, and is bounded on one side by the chloride ions in the structure.

A larger supercell was created with composition $\text{Li}_{104}\text{Al}_{24}\text{S}_{80}\text{Cl}_{16}$ and was used for a 100 ps *ab initio* MD run at 400 K. The trajectories of the Li ions throughout the production run are shown in Figure 5a,b. Figure 5b shows that some site-to-site Li hopping occurs within the “Li-only layer” from one octahedral site to another, through the intermediate tetrahedral site (yellow) with which it shares a common face. This corresponds to Li2-Li3-Li2 hops (O-T-O).

Moreover, some site-to-site hopping is observed across the tetrahedral layer (Figure 5a, bottom right, orange to blue) involving Li3-Li1 as well as Li1-Li1 hops and suggesting that the transport may not be solely two-dimensional. The Li1-Li1 hops (green to yellow on Figure 5a) seem to happen much less frequently than the Li2-Li3 and Li1-Li3 hops, which indicates higher activation energy involved in the tetrahedral to tetrahedral jumps. Interestingly, this observation strongly differs with the Li trajectories obtained in the related structure $\text{Li}_{4.4}\text{Al}_{0.4}\text{Ge}_{0.6}\text{S}_4$, for which 2D diffusion within the octahedral layer only was determined through a combined NMR and AIMD analysis.³⁴ As explained in part 3.2, $\text{Li}_{4.4}\text{Al}_{0.4}\text{Ge}_{0.6}\text{S}_4$ presents a more ordered structure with differentiation of the Ge/Al and Li tetrahedral sites, and the presence of ordered octahedral vacancies in the octahedral layer. Tetrahedral to tetrahedral jumps were identified for Cu^+ cations through AIMD in the wurtzite material CuI, where all copper atoms are located in tetrahedral sites.⁴⁷ In both $\text{Li}_{4.3}\text{Al}_{3.3}\text{S}_{3.3}\text{Cl}_{0.7}$ and CuI, long range diffusion along the c axis is made possible thanks to O(Li2)-T(Li3)-T(Li1)-T(Li1)-T(Li3)-O(Li2) and to T(Cu)-T(Cu) hops, respectively. Octahedral to octahedral hops, which would also enable long range diffusion along the c axis, are not observed in any of these materials.

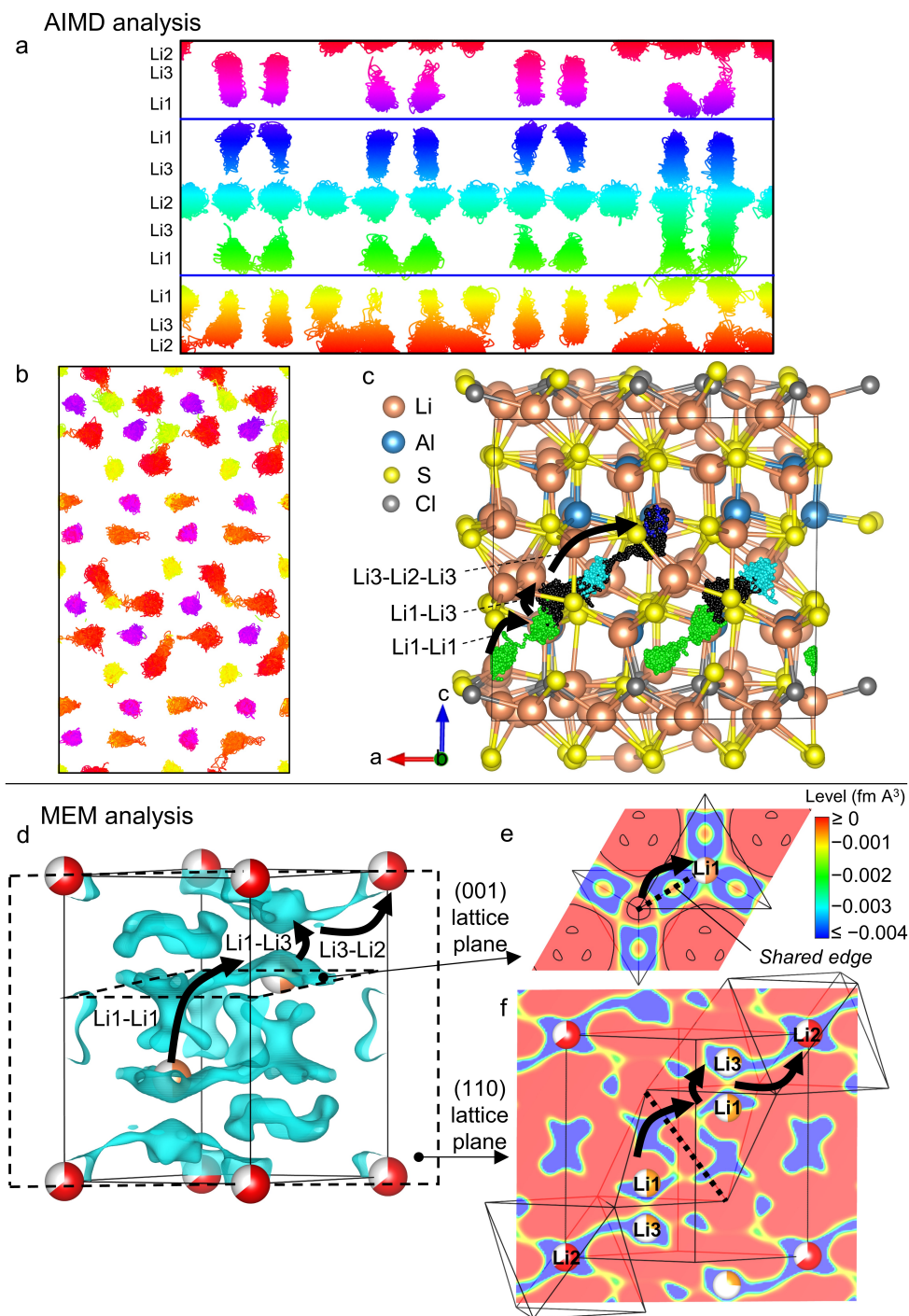


Figure 5. Visualization of Li diffusion pathways using AIMD (a, b and c) and MEM (d, e, f). (a) and (b) Positions of Li ions within the $\text{Li}_{104}\text{Al}_{24}\text{S}_{80}\text{Cl}_{16}$ supercell over a 100 ps AIMD trajectory. Atoms are colored according to their position along the c axis. (a) View along the a axis. The cell is split into two halves using the heights shown with blue lines. (b) The cell is viewed down the c axis showing the half of the cell centered on the octahedral layer at the bottom/top of the cell. (c) View of five Li atoms in the structure throughout their AIMD trajectory. The mobile Li atoms are colored according to which site they belong, as in (a): green and blue for Li1, cyan for Li2, an exception is made for Li3, colored in black, in order to distinguish it more clearly. The other atoms are frozen in the positions they have at the start of the AIMD production run. (d, e, f) Nuclear density reconstructed by the maximum entropy method using Bank 5 of the ND data of $\text{Li}_{4.3}\text{AlS}_{3.3}\text{Cl}_{0.7}$ and highlighted potential diffusion pathways, matching those observed with AIMD on (b). (d) 3D Isosurface of the negative nuclear density within the cell (level = -0.004 fm A^3), (e) 2D nuclear density map in the (001) plane passing through Li1, (f) 2D nuclear density map in the (110) plane passing through Li2, Li3 and Li1.

The influence of disorder on the conductivity dimensionality was further examined with AIMD using the structure of $\text{Li}_{4.4}\text{Al}_{0.4}\text{Ge}_{0.6}\text{S}_4$ as a starting point (Figure S3e) while keeping the $\text{Li}_{4.3}\text{AlS}_{3.3}\text{Cl}_{0.7}$ composition. The ordered octahedral vacant sites and Li/Al ordering within the tetrahedral layer were kept from $\text{Li}_{4.4}\text{Al}_{0.4}\text{Ge}_{0.6}\text{S}_4$ with the S/Cl and Li site disorder introduced to match $\text{Li}_{4.3}\text{AlS}_{3.3}\text{Cl}_{0.7}$. The optimized and lowest energy structure is presented on Figure S9. A supercell with composition $\text{Li}_{104}\text{Al}_{24}\text{S}_{80}\text{Cl}_{16}$ was constructed and used for a 100 ps AIMD production run at 400 K. The trajectory of Li ions during the run are shown in Figure S10. The octahedral sites (purple in Figure S10b and light green in Figure S10c) do not show any site-to-site hopping. Some isolated hopping events do appear to happen from tetrahedral sites into the vacant octahedral sites and back (e.g. pink Li at top center of Figure S10b). However, on the contrary to Li1-Li1 hops observed in the model with the experimental structure, no hopping of tetrahedral Li to tetrahedral Li within the tetrahedral layer can be seen. This comparison highlights the importance of a higher degree of atomic disorder for accessing more diverse hopping pathways.

Further visualization of the 3-dimensional Li diffusion pathways in the disordered $\text{Li}_{4.3}\text{AlS}_{3.3}\text{Cl}_{0.7}$ was performed by tracking the position of five different selected Li atoms over a 100 ps period, showing their movement throughout the trajectory (Figure 5c). The Li atoms are colored according to which site they belong. Diffusion within and across the tetrahedral layer is clearly identified with Li1-Li1 hops through their shared edge (green) followed by Li1-Li3 exchange across the shared tetrahedral face (green-black). Consecutively, diffusion within the “Li-only” layer is observed with Li3-Li2-Li3 hops (black-cyan-black) occurring via the shared octahedral-tetrahedral faces. Furthermore, these three hopping events happen simultaneously, leading to a knock-on mechanism responsible for concerted migration of Li within the structure. This mechanism is different from the classical direct hopping mechanism, where isolated Li hop events

happen through empty interstices, and has been shown to be responsible for fast ionic conductivity in different types of materials.⁴⁸

Experimental evidence for Li diffusion pathway was obtained through the analysis of the nuclear density maps derived from neutron diffraction data using the Maximum Entropy Method (MEM, *cf.* Experimental Section). Figure 5d shows the nuclear density isosurface map within the $\text{Li}_{4.3}\text{AlS}_{3.3}\text{Cl}_{0.7}$ cell. Visualization of negative levels is performed enabling to distinguish Li positions (^7Li scattering length is negative: $b_{\text{Li}} = -2.22$ fm) and identify hopping pathways. These are marked with arrows on Figure 5d, e, f and are in perfect accordance with pathways obtained from AIMD: Li1-Li1 hops through their shared edge (dotted line on Figure 5e, f), Li1-Li3 hops through the shared face and Li3-Li2 hops through the common tetrahedral-octahedral face. The comparison between AIMD and MEM analysis applied to the same material is rarely performed in the literature. The theoretical AIMD method models the dynamic evolution of a local environment, thereby giving a direct the trajectory of atoms, and the MEM analysis gives an average nuclear density within a crystal cell, thereby showing places where Li atoms should be. Here, the exact correspondence between results shows that it is possible to link experimental data of the average structure to a detailed understanding of local motion.

4. Discussion

The substitution of sulfide for chloride anions into the pure sulfide materials Li_3AlS_3 and Li_5AlS_4 leads to the formation of a new phase, showing major differences in its structure and Li conductivity properties.

First, while the substitution maintains the two layers type arrangement (tetrahedral Li/Al layers alternating with “Li-only” layers, in between anion slabs packed in a *hcp* manner), it generates a

high degree of atomic disorder. This disorder is observed both in the anionic sublattice (through a random occupancy of the anion site by S^{2-} and Cl^-) and within the cationic sublattice with a random occupancy of Al and Li in the tetrahedral sites, as well as the partial occupancy of the octahedral sites, leading to the presence of disordered vacancies to the amount of 35.6(2) %. The observation that anion doping leads to a disordered structure has been reported in the literature in various type of compounds¹²⁻¹⁷ although the origin for this structural behavior remains unclear. By calculating the stabilization temperature of disordered and ordered structures in both chloride-substituted and non-substituted materials, we prove that the structure is thermodynamically stabilized by the presence of Cl. Indeed, it cannot be explained by kinetic consideration on their own, such as differences in the reaction kinetics of the starting materials. Thermodynamic stabilization of the disordered structure could be explained by the increase in configurational entropy brought by the insertion of a second chemical element on the same atomic site or by the randomization of interstitial site geometries.

Secondly, Cl substituted materials show major differences in the conductivity properties compared to the related pure sulfide materials. The conductivity values are increased by a factor 10^3 compared to the ordered sulfide phases Li_3AlS_3 and Li_5AlS_4 ,^{22,23} but is of the same order to magnitude as $Li_{4.4}M_{0.4}M'_{0.6}S_4$ ($M = Al, Ga; M' = Ge, Sn$).³⁴ The latter presents some Li site vacancies while maintaining an ordered M/M' vs. Li site arrangement and the presence of ordered octahedral vacancies. This increase in conductivity is attributed to the presence of disordered vacancies in both types of materials, absent in the ternary compounds.

Further insight in the limiting transport mechanism is given through the comparison of diffusion pathways in fully disordered $Li_{4.3}AlS_{3.3}Cl_{0.7}$ (modeled using the experimental structure) and in the partially disordered $Li_{4.3}AlS_{3.3}Cl_{0.7}$ (modeled using the $Li_{4.4}Al_{0.4}Ge_{0.6}S_4$ structure). It suggests that

introducing more disorder in $\text{Li}_{4.3}\text{AlS}_{3.3}\text{Cl}_{0.7}$, *ie.* Li/Al site disorder in the tetrahedral layer and fully disordered octahedral vacancies, enables to access 3D hopping pathways, favorable for enhanced Li conductivity. This effect cannot be attributed to the presence of Cl only, nor to the modification in the local geometry of atoms, as these two effects are kept unchanged in both models. Rather, this could find its origin in the increased entropy of the material, which has a fundamental effect on the ion dynamics. From a certain level of disorder, migration involves several particles at the same time: the movement of one ion automatically results in that of one or more others in response.^{49,50} The activation of this concerted ion migration mechanism is therefore sought to increase ionic conductivity.⁵¹ One explanation for obtaining this type of mechanism is the occupation, by the mobile ion, of both a high-energy site and a more stable low energy site. This has the effect of reducing the potential barrier as the ion jumps from the high energy site to the low energy site and activates the concerted jump mechanism.⁴⁸ This mechanism is observed with AIMD in $\text{Li}_{4.3}\text{AlS}_{3.3}\text{Cl}_{0.7}$ and is schematized on Figure 6. Li3 is believed to be less stable than the other two sites given its lower *sof*, therefore, the apparent activation energy for Li1-Li1 hops (E_{a3D} on Figure 6a) will be lowered compared to an isolated jump. On the contrary, 2D diffusion involving Li2-Li3-Li2 jumps does not benefit from concerted migration, as both starting and ending states have the same energy (Figure 6b).

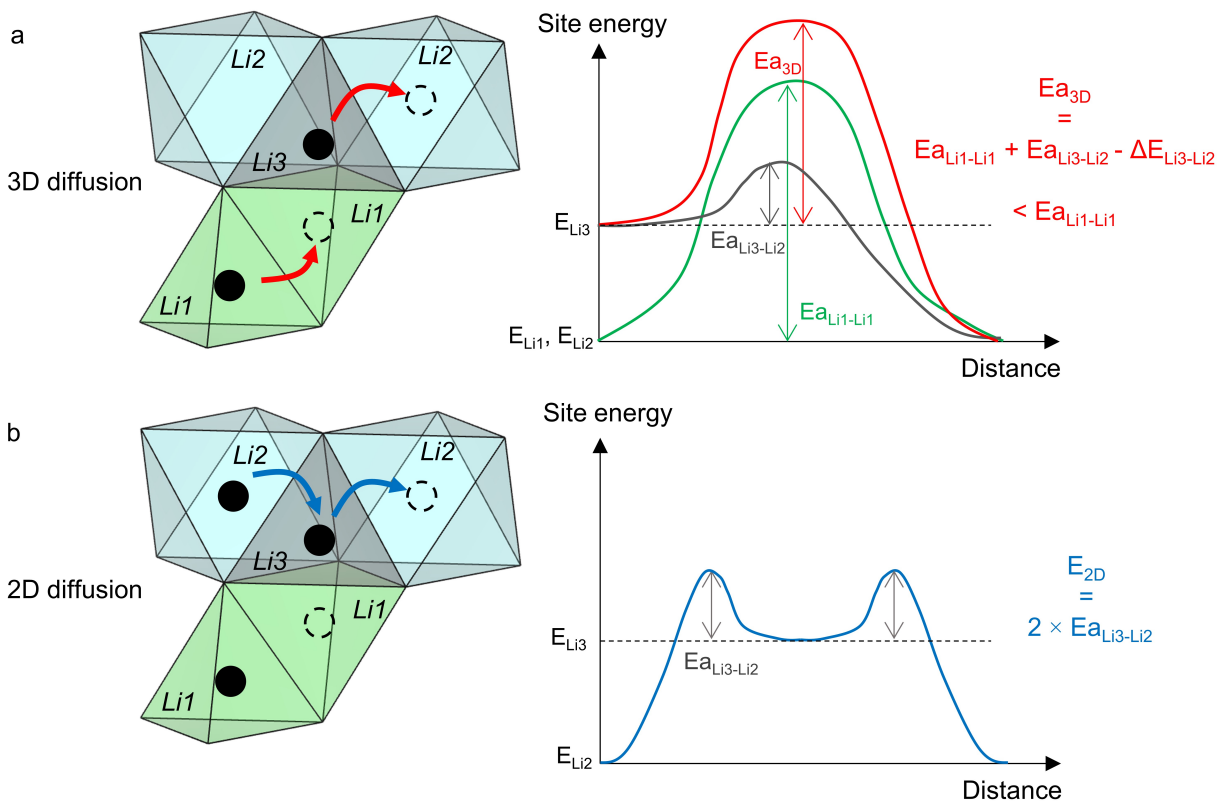


Figure 6. Activation energies involved in the 3D (a) and 2D (b) diffusion processes in $\text{Li}_{4.3}\text{AlS}_{3.3}\text{Cl}_{0.7}$. 3D diffusion is triggered thanks to a concerted migration mechanism decreasing the apparent activation energy for Li1-Li1 hops.

In both 2D and 3D diffusion processes, Li mobility can be limited by either the absence of a vacancy in the Li2 site, or by a too high energy barrier to overcome. In $\text{Li}_{4.3}\text{AlS}_{3.3}\text{Cl}_{0.7}$, the number of vacancies per Li2 octahedra is 0.356(2), which corresponds to ~ 4.2 vacancies per nm^3 . In comparison, in $\text{Li}_{4.4}\text{Al}_{0.4}\text{Ge}_{0.6}\text{S}_4$, the number of disordered vacancies is ~ 1.1 vacancies per nm^3 ,³⁴ yet, it shows a higher conductivity, suggesting that the number of disordered vacancies is not the limiting factor Li mobility in $\text{Li}_{4.3}\text{AlS}_{3.3}\text{Cl}_{0.7}$. We can therefore deduce that the activation energy involving O-T-O jumps in the octahedral layer is higher than in $\text{Li}_{4.4}\text{Al}_{0.4}\text{Ge}_{0.6}\text{S}_4$, and that this barrier is limiting conductivity. This could be explained by the presence of Cl^- anions, with higher electronegativity and hence lower polarizability than S^{2-} , thereby decreasing the overall Li bond covalency. In $\text{Li}_{4.3}\text{AlS}_{3.3}\text{Cl}_{0.7}$, the positive effect of disorder leading to 3D diffusion pathways in

counterbalanced by a high activation energy, but is not limited by the number of disordered vacancies.

In order to further increase conductivity in this structure type, one must take advantage of both effects: 3D diffusivity and low activation energy. For instance, heterovalent doping with on either the anionic (with higher polarizable anions such as Br^- , I^-) or the cationic sites could be interesting to increase Li bond covalency, enlarge the unit cell volume and open wider bottleneck, while maintaining the high degree of atomic disorder, necessary for 3D conductivity.

5. Conclusion

A novel sulfide chloride phase was identified in the Li-Al-S-Cl phase diagram, with composition spanning $\text{Li}_{5-y}\text{Al}_{1+(y-x)/3}\text{S}_{4-x}\text{Cl}_x$ ($x = 0.5 - 0.7$; $y = 0.5 - 1$). Its structure resembles that of Li_2FeS_2 and can be described as a disordered analogue to that of the parent sulfide phases Li_3AlS_3 and Li_5AlS_4 , while maintaining the two layers type arrangement (tetrahedral layers alternating with “Li-only” polyhedral layers). The thermodynamic stabilization of this high symmetry phase and the presence of large atomic disorder was facilitated thanks to the introduction of chloride anion on the sulfur site, as revealed by phase stability calculations. In depth crystallographic characterization was performed on $\text{Li}_{4.3}\text{AlS}_{3.3}\text{Cl}_{0.7}$ ($x = 0.7$; $y = 0.7$) by means of combined high-resolution X-ray and neutron diffraction together with NMR spectroscopy. Neutron diffraction in particular enabled to reveal major differences in the lithium site position and occupation compared to the sulfide phases, with the localization of disordered vacancies among the octahedral sites only as well as the splitting of tetrahedral lithium atoms. A combined experimental-theoretical approach revealed the major impact of these defects on the conductivity properties, as both take part in the main diffusion pathway, in turns leading to an increase of 3 orders of magnitude in the Li conductivity.

Remarkably, AIMD and MEM evidenced exactly the same Li hopping paths. This directly supports the relevance of using MEM associated with neutron diffraction to determine diffusion pathways from experimental data. Moreover, a correlation is made between high atomic disorder and the access to a 3D conductivity pathway, which was revealed for the first time in this structure type. By defining the limiting conductivity mechanism and analyzing the strong impact of chlorine for sulfur substitution, we highlight a path for the exploration of new promising mixed anion Li electrolyte materials.

ASSOCIATED CONTENT

Supporting Information. Structural information on the four “phase A” compositions (SRXD patterns, lattice parameters and cell volume), Laboratory XRD patterns of additional impure sample within the Li-Al-S-Cl phase field, Comparison of the crystal structures of $\text{Li}_{4.3}\text{AlS}_{3.3}\text{Cl}_{0.7}$, Li_2FeS_2 , Li_5AlS_4 , Li_3AlS_3 and $\text{Li}_{4.4}\text{Al}_{0.4}\text{Ge}_{0.6}\text{S}_{4.4}$, Preliminary Rietveld refinement and Fourier difference map of $\text{Li}_{4.3}\text{AlS}_{3.3}\text{Cl}_{0.7}$, Final Rietveld fit against the NPD data from Bank 3 and Bank 4, Summary of the outcome of the refinement, Crystal structure of $\text{Li}_{4.3}\text{AlS}_{3.3}\text{Cl}_{0.7}$, ΔG vs. temperature plots, Structural models used for AIMD, AIMD trajectories in the hypothetical partially ordered structure of $\text{Li}_{4.3}\text{AlS}_{3.3}\text{Cl}_{0.7}$. Associated structural information of $\text{Li}_{4.3}\text{AlS}_{3.3}\text{Cl}_{0.7}$ are available from the Cambridge Structural Database (CSD deposition number 2050422).

AUTHOR INFORMATION

Corresponding Author

* M.J.Rosseinsky@liverpool.ac.uk

Author Contributions

The manuscript was written through contributions of all authors. All authors have given approval to the final version of the manuscript.

Funding Sources

EPSRC funding under EP/N004884 and EP/S0133393/1, Leverhulme Research Centre for Functional Materials Design, ISCF Faraday Challenge project.

Notes

The authors declare no competing financial interest.

ACKNOWLEDGMENT

We thank EPSRC for funding under EP/N004884 and EP/S0133393/1. MWG thanks the Leverhulme Trust for funding via the Leverhulme Research Centre for Functional Materials Design. We are grateful for computational support from the UK Materials and Molecular Modelling Hub, which is partially funded by EPSRC (EP/P020194). We acknowledge the ISCF Faraday Challenge project: “SOLBAT – The Solid-State (Li or Na) Metal-Anode Battery” including partial support of a studentship to BBD, also supported by the University of Liverpool. We thank Diamond Light Source for access to beamline I11, Prof. Chiu Tang, and Dr. Claire Murray for assistance on the beamline. We thank STFC for access to Polaris instrument (Xpress proposals XB1890391), Dr R. I. Smith for running the measurements.

REFERENCES

- (1) Nitta, N.; Wu, F.; Lee, J. T.; Yushin, G. Li-Ion Battery Materials: Present and Future. *Materials Today* **2015**, *18* (5), 252–264.
- (2) Jeong, G.; Kim, Y.-U.; Kim, H.; Kim, Y.-J.; Sohn, H.-J. Prospective Materials and Applications for Li Secondary Batteries. *Energy & Environmental Science* **2011**, *4*, 1986–2002.

- (3) Ye, T.; Li, L.; Zhang, Y. Recent Progress in Solid Electrolytes for Energy Storage Devices. *Advanced Functional Materials* **2020**, *30* (29), 2000077.
- (4) Lau, J.; DeBlock, R. H.; Butts, D. M.; Ashby, D. S.; Choi, C. S.; Dunn, B. S. Sulfide Solid Electrolytes for Lithium Battery Applications. *Adv. Energy Mater.* **2018**, *8* (27), 1800933.
- (5) Manthiram, A.; Yu, X.; Wang, S. Lithium Battery Chemistries Enabled by Solid-State Electrolytes. *Nat Rev Mater* **2017**, *2* (4), 1–16.
- (6) Buannic, L.; Orayech, B.; López Del Amo, J.-M.; Carrasco, J.; Katcho, N. A.; Aguesse, F.; Manalastas, W.; Zhang, W.; Kilner, J.; Llordés, A. Dual Substitution Strategy to Enhance Li⁺ Ionic Conductivity in Li₇La₃Zr₂O₁₂ Solid Electrolyte. *Chem. Mater.* **2017**, *29* (4), 1769–1778.
- (7) Seino, Y.; Ota, T.; Takada, K.; Hayashi, A.; Tatsumisago, M. A Sulphide Lithium Super Ion Conductor Is Superior to Liquid Ion Conductors for Use in Rechargeable Batteries. *Energy Environ. Sci.* **2014**, *7* (2), 627–631.
- (8) Kato, Y.; Hori, S.; Saito, T.; Suzuki, K.; Hirayama, M.; Mitsui, A.; Yonemura, M.; Iba, H.; Kanno, R. High-Power All-Solid-State Batteries Using Sulfide Superionic Conductors. *Nat Energy* **2016**, *1* (4), 1–7.
- (9) Asano, T.; Sakai, A.; Ouchi, S.; Sakaida, M.; Miyazaki, A.; Hasegawa, S. Solid Halide Electrolytes with High Lithium-Ion Conductivity for Application in 4 V Class Bulk-Type All-Solid-State Batteries. *Advanced Materials* **2018**, *30* (44), 1803075.
- (10) Harada, J. K.; Charles, N.; Poeppelmeier, K. R.; Rondinelli, J. M. Heteroanionic Materials by Design: Progress Toward Targeted Properties. *Advanced Materials* **2019**, *31* (19), 1805295.
- (11) Kageyama, H.; Hayashi, K.; Maeda, K.; Attfield, J. P.; Hiroi, Z.; Rondinelli, J. M.; Poeppelmeier, K. R. Expanding Frontiers in Materials Chemistry and Physics with Multiple Anions. *Nature Communications* **2018**, *9* (1), 772.
- (12) Feng, X.; Chien, P.-H.; Patel, S.; Wang, Y.; Hu, Y.-Y. Enhanced Ion Conduction in Li_{2.5}Zn_{0.25}PS₄ via Anion Doping. *Chem. Mater.* **2020**.
- (13) Lee, Y.-S.; Ley, M. B.; Jensen, T. R.; Cho, Y. W. Lithium Ion Disorder and Conduction Mechanism in LiCe(BH₄)₃Cl. *J. Phys. Chem. C* **2016**, *120* (34), 19035–19042.
- (14) Tarasova, N. A.; Animitsa, I. E. Effect of Anion Doping on Mobility of Ionic Charge Carriers in Solid Solutions Based on Ba₂In₂O₅. *Russ J Electrochem* **2013**, *49* (7), 698–703.
- (15) Kong, S.-T.; Deiseroth, H.-J.; Reiner, C.; Gün, Ö.; Neumann, E.; Ritter, C.; Zahn, D. Lithium Argyrodites with Phosphorus and Arsenic: Order and Disorder of Lithium Atoms, Crystal Chemistry, and Phase Transitions. *Chemistry – A European Journal* **2010**, *16* (7), 2198–2206.
- (16) Olsen, J. E.; Karen, P.; Sørby, M. H.; Hauback, B. C. Effect of Chloride Substitution on the Order–Disorder Transition in NaBH₄ and Na₁₁BD₄. *Journal of Alloys and Compounds* **2014**, *587*, 374–379.

- (17) Cuan, J.; Zhou, Y.; Zhou, T.; Ling, S.; Rui, K.; Guo, Z.; Liu, H.; Yu, X. Borohydride-Scaffolded Li/Na/Mg Fast Ionic Conductors for Promising Solid-State Electrolytes. *Advanced Materials* **2019**, *31* (1), 1803533.
- (18) Morscher, A.; Dyer, M. S.; Duff, B. B.; Han, G.; Gamon, J.; Daniels, L. M.; Dang, Y.; Surta, T. W.; Robertson, C. M.; Blanc, F.; Claridge, J. B.; Rosseinsky, M. J. Li₆SiO₄Cl₂: A Hexagonal Argyrodite Based on Antiperovskite Layer Stacking. *Chem. Mater.* **2021**, *33* (6), 2206–2217.
- (19) Bates, J. B.; Dudney, N. J.; Gruzalski, G. R.; Zuhr, R. A.; Choudhury, A.; Luck, C. F.; Robertson, J. D. Electrical Properties of Amorphous Lithium Electrolyte Thin Films. *Solid State Ionics* **1992**, *53–56*, 647–654.
- (20) Yu, X.; Bates, J. B.; Jellison, G. E.; Hart, F. X. A Stable Thin-Film Lithium Electrolyte: Lithium Phosphorus Oxynitride. *J. Electrochem. Soc.* **1997**, *144* (2), 524.
- (21) Lian, P.-J.; Zhao, B.-S.; Zhang, L.-Q.; Xu, N.; Wu, M.-T.; Gao, X.-P. Inorganic Sulfide Solid Electrolytes for All-Solid-State Lithium Secondary Batteries. *J. Mater. Chem. A* **2019**, *7* (36), 20540–20557.
- (22) Lim, H.; Kim, S.-C.; Kim, J.; Kim, Y.-I.; Kim, S.-J. Structure of Li₅AlS₄ and Comparison with Other Lithium-Containing Metal Sulfides. *Journal of Solid State Chemistry* **2018**, *257*, 19–25.
- (23) Gamon, J.; Duff, B. B.; Dyer, M. S.; Collins, C.; Daniels, L. M.; Surta, T. W.; Sharp, P. M.; Gaultois, M. W.; Blanc, F.; Claridge, J. B.; Rosseinsky, M. J. Computationally Guided Discovery of the Sulfide Li₃AlS₃ in the Li–Al–S Phase Field: Structure and Lithium Conductivity. *Chem. Mater.* **2019**, *31* (23), 9699–9714.
- (24) FullProf Suite - Crystallographic Tool for Rietveld, Profile Matching & Integrated Intensity Refinements of X-Ray and/or Neutron Data, <http://www.ill.eu/sites/fullprof/>.
- (25) Béjar, J.-F.; Lelann, P. E.s.d.'s and Estimated Probable Error Obtained in Rietveld Refinements with Local Correlations. *J Appl Cryst* **1991**, *24* (1), 1–5.
- (26) Johnson, D. ZView: A Software Program for IES Ana;Ysis 3.5d. Scribner Associates Inc. 2007.
- (27) Ales Medek, John S. Harwood, and L. F. Multiple-Quantum Magic-Angle Spinning NMR: A New Method for the Study of Quadrupolar Nuclei in Solids. *J. Am. Chem. Soc* **1995**, *117* (51), 12779–12787.
- (28) Amoureux, J. P.; Fernandez, C.; Steuernagel, S. Z Filtering in MQMAS NMR. *Journal of Magnetic Resonance - Series A* **1996**, *123* (1), 116–118.
- (29) Kresse, G.; Hafner, J. Ab Initio Molecular Dynamics for Liquid Metals. *Phys. Rev. B* **1993**, *47* (1), 558–561.
- (30) Perdew, J. P.; Burke, K.; Ernzerhof, M. Generalized Gradient Approximation Made Simple. *Phys. Rev. Lett.* **1996**, *77* (18), 3865–3868.
- (31) Okhotnikov, K.; Charpentier, T.; Cadars, S. Supercell Program: A Combinatorial Structure-Generation Approach for the Local-Level Modeling of Atomic Substitutions and Partial Occupancies in Crystals. *Journal of Cheminformatics* **2016**, *8* (1), 17.

- (32) Enciso-Maldonado, L.; Dyer, M. S.; Jones, M. D.; Li, M.; Payne, J. L.; Pitcher, M. J.; Omir, M. K.; Claridge, J. B.; Blanc, F.; Rosseinsky, M. J. Computational Identification and Experimental Realization of Lithium Vacancy Introduction into the Olivine LiMgPO₄. *Chem. Mater.* **2015**, *27* (6), 2074–2091.
- (33) Kresse, G.; Furthmüller, J. Efficient Iterative Schemes for Ab Initio Total-Energy Calculations Using a Plane-Wave Basis Set. *Phys. Rev. B* **1996**, *54* (16), 11169–11186.
- (34) Leube, B. T.; Inglis, K. K.; Carrington, C.-G. D. of L.; Sharp, P. M.; Shin, J. F.; Neale, A. R.; Manning, T. D.; Pitcher, M. J.; Hardwick, L. J.; Dyer, M. S.; Blanc, F.; Claridge, J. B.; Rosseinsky, M. J. Lithium Transport in Li_{4.4}M_{0.4}M'_{0.6}S₄ (M = Al³⁺, Ga³⁺, and M' = Ge⁴⁺, Sn⁴⁺): Combined Crystallographic, Conductivity, Solid State NMR, and Computational Studies. *Chem. Mater.* **2018**, *30* (20), 7183–7200.
- (35) Nosé, S. A Unified Formulation of the Constant Temperature Molecular Dynamics Methods. *J. Chem. Phys.* **1984**, *81* (1), 511–519.
- (36) Momma, K.; Izumi, F. *Evaluation of Algorithms and Weighting Methods for MEM Analysis from Powder Diffraction Data*; De Gruyter, 2011; pp 195–200.
- (37) Smaalen, S. van; Palatinus, L.; Schneider, M. The Maximum-Entropy Method in Superspace. *Acta Crystallographica Section A: Foundations of Crystallography* **2003**, *59* (5), 459–469.
- (38) Nishimura, S.; Kobayashi, G.; Ohoyama, K.; Kanno, R.; Yashima, M.; Yamada, A. Experimental Visualization of Lithium Diffusion in Li_xFePO₄. *Nature Materials* **2008**, *7* (9), 707–711.
- (39) Weber, D. A.; Senyshyn, A.; Weldert, K. S.; Wenzel, S.; Zhang, W.; Kaiser, R.; Berendts, S.; Janek, J.; Zeier, W. G. Structural Insights and 3D Diffusion Pathways within the Lithium Superionic Conductor Li₁₀GeP₂S₁₂. *Chem. Mater.* **2016**, *28* (16), 5905–5915.
- (40) Yashima, M.; Nomura, K.; Kageyama, H.; Miyazaki, Y.; Chitose, N.; Adachi, K. Conduction Path and Disorder in the Fast Oxide-Ion Conductor (La_{0.8}Sr_{0.2})(Ga_{0.8}Mg_{0.15}Co_{0.05})O_{2.8}. *Chemical Physics Letters* **2003**, *380* (3), 391–396.
- (41) Momma, K.; Ikeda, T.; Belik, A. A.; Izumi, F. Dysnomia, a Computer Program for Maximum-Entropy Method (MEM) Analysis and Its Performance in the MEM-Based Pattern Fitting. *Powder Diffraction* **2013**, *28* (3), 184–193.
- (42) Momma, K.; Izumi, F. VESTA 3 for Three-Dimensional Visualization of Crystal, Volumetric and Morphology Data. *J Appl Cryst* **2011**, *44* (6), 1272–1276.
- (43) Shannon, R. t. Revised Effective Ionic Radii and Systematic Studies of Interatomic Distances in Halides and Chalcogenides. *Acta Crystallographica Section A: Crystal Physics, Diffraction, Theoretical and General Crystallography* **1976**, *32* (5), 751–767.
- (44) Batchelor, R. J.; Einstein, F. W. B.; Jones, C. H. W.; Fong, R.; Dahn, J. R. Crystal Structure of Li₂FeS₂. *Phys. Rev. B* **1988**, *37* (7), 3699–3702.
- (45) Meyer, B. M.; Leifer, N.; Sakamoto, S.; Greenbaum, S. G.; Grey, C. P. High Field Multinuclear NMR Investigation of the SEI Layer in Lithium Rechargeable Batteries. *Electrochemical and Solid-State Letters* **2005**, *8* (3).

- (46) Smith, M. E.; van Eck, E. R. H. Recent Advances in Experimental Solid State NMR Methodology for Half-Integer Spin Quadrupolar Nuclei. *Progress in Nuclear Magnetic Resonance Spectroscopy* **1999**, *34* (2), 159–201.
- (47) Zheng-Johansson, J. A Molecular Dynamics Study of Ionic Conduction in CuI. II. Local Ionic Motion and Conduction Mechanisms. *Solid State Ionics* **1996**, *83* (1–2), 35–48.
- (48) He, X.; Zhu, Y.; Mo, Y. Origin of Fast Ion Diffusion in Super-Ionic Conductors. *Nat Commun* **2017**, *8* (1), 1–7.
- (49) Funke, K. Broadband Conductivity Spectroscopy for Studying the Dynamics of Mobile Ions in Materials with Disordered Structures. In *Methods in Physical Chemistry*; John Wiley & Sons, Ltd, 2012; pp 191–229.
- (50) Funke, K.; Banhatti, R. D. Ionic Motion in Materials with Disordered Structures. *Solid State Ionics* **2006**, *177* (19), 1551–1557.
- (51) Xiong, S.; He, X.; Han, A.; Liu, Z.; Ren, Z.; McElhenny, B.; Nolan, A. M.; Chen, S.; Mo, Y.; Chen, H. Computation-Guided Design of LiTaSiO₅, a New Lithium Ionic Conductor with Spinel Structure. *Advanced Energy Materials* **2019**, *9* (22), 1803821.